HAL
open science

# Coherent x-ray scattering in an XPEEM setup

T.O. Menteş, F. Genuzio, V. Schánilec, J. Sadílek, Nicolas Rougemaille, A. Locatelli

## To cite this version:

T.O. Menteş, F. Genuzio, V. Schánilec, J. Sadílek, Nicolas Rougemaille, et al.. Coherent x-ray scattering in an XPEEM setup. Ultramicroscopy, 2020, 216, pp.113035. 10.1016/j.ultramic.2020.113035 . hal-02963798

**HAL Id: hal-02963798**

**https://hal.science/hal-02963798v1**

Submitted on 11 Oct 2020

**HAL** is a multi-disciplinary open access archive for the deposit and dissemination of scientific research documents, whether they are published or not. The documents may come from teaching and research institutions in France or abroad, or from public or private research centers.

L'archive ouverte pluridisciplinaire **HAL**, est destinée au dépôt et à la diffusion de documents scientifiques de niveau recherche, publiés ou non, émanant des établissements d'enseignement et de recherche français ou étrangers, des laboratoires publics ou privés.

# Coherent x-ray scattering in an XPEEM setup

T. O. Menteş[a], F. Genuzio[a], V. Schánilec[b], N. Rougemaille[b], M. Kiskinova[a], A. Locatelli[a]

[a]*Sincrotrone Trieste S.C.p.A., Basovizza-Trieste 34149, Italy*
[b]*CNRS, Inst NÉEL, Grenoble, F-38000, France*

**Abstract**

X-ray photoemission electron microscopy has been one of the most productive x-ray microscopy tools with chemical and magnetic sensitivity. We demonstrate that an existing XPEEM setup can be readily adapted to simultaneously perform coherent x-ray scattering measurements in reflectivity mode. Photon-in photon-out x-ray scattering measurement provides the sensitivity to buried interfaces as well as the possibility to work under external fields not accessible in an electron-based measurement. XPEEM, in turn, greatly alleviates the difficulties associated with the reconstruction methods used in coherent diffraction imaging. The combination of the two methods is demonstrated for a spin-ice lattice showing both chemical and magnetic contrast.

*Keywords:*
XPEEM, speckle, CDI, reconstruction, resonant x-ray scattering, LEEM

## 1. Introduction

The first studies leading to the x-ray Coherent Diffraction Imaging (CDI) took place years before it was established as an imaging method [1, 2]. Due

*Email address:* mentest@elettra.trieste.it (T. O. Menteş)

to the requirements on the lateral coherence of the illuminating x-ray beam, the development of the technique had to closely follow that of high brightness synchrotron sources. Thus, the first experimental demonstration of imaging an extended object using CDI took place just before the turn of century decades after its conception [3].

In obtaining the real-space reconstruction, the phase problem, inherent in the measurement of diffraction amplitudes, was first tackled by using oversampling ideas dating back to 1950's [4]. This was followed by a variety of approaches including iterative algorithms to retrieve the missing phases, wavefront propagation in the near field, ptychography and holography [5]. Nevertheless, the image reconstruction still remains as the limiting factor in trying to establish CDI as a generally-applicable imaging method. In order to overcome the difficulties presented by the missing phase problem, almost all the approaches make use of different beam defining, filtering, focusing or referencing optics. These elements are commonly placed in the near-field of the sample, typically within a few mm's. As a result, transmission geometry using adequately thin samples provides a more convenient experimental configuration, though at the same time greatly limiting the samples that can be investigated.

In this respect, demonstration of CDI in reflection geometry, both using laser [6] and x-ray sources [7], has been an important step towards making it applicable in a more general context. It should be underlined that the reflection at incidence angles away from the surface normal approaching grazing geometry introduces further considerations, among which those due to the surface roughness and the elongated beam footprint can be counted. On

the other hand, recent studies taking advantage of the element selectivity in coherent x-ray scattering at selected absorption thresholds show that the information coded in the diffraction pattern can be put to use even without the need for a real-space reconstruction [8].

Along these lines, we describe the possibility to implement coherent x-ray scattering measurements in reflection mode within an X-ray PhotoEmission Electron Microscope (XPEEM). The high spatial resolution chemical and magnetic imaging capability of the XPEEM instrument is complemented by the depth sensitivity and the compatibility with external fields of the photon-in/photon-out x-ray diffraction process. The feasibility and the usefulness of simultaneous photoemission and x-ray diffraction measurements are demonstrated using a lithographically-made spin-ice lattice showing chemical and magnetic heterogeneity at length scales below 1 micron.

## 2. Experimental setup

### *2.1. Undulator beamline*

The experiments were carried out at the soft x-ray beamline Nanospectroscopy at Elettra (Sincrotrone Trieste, Italy) as sketched in Fig. 1. The beamline has two undulator sources with elliptical polarization and a varied-line spacing (VLS) grating monochromator [9, 10]. The APPLE-2 type undulators are made of periodic arrays of permanent magnets. By mechanically shifting different sections of the magnet arrays, the APPLE-2 type undulator can provide linear horizontal, linear vertical and circularly polarized x-rays from 10 eV up to 1000 eV [11]. The two identical undulators are separated by an electromagnet to match their phases. The undulators are followed by

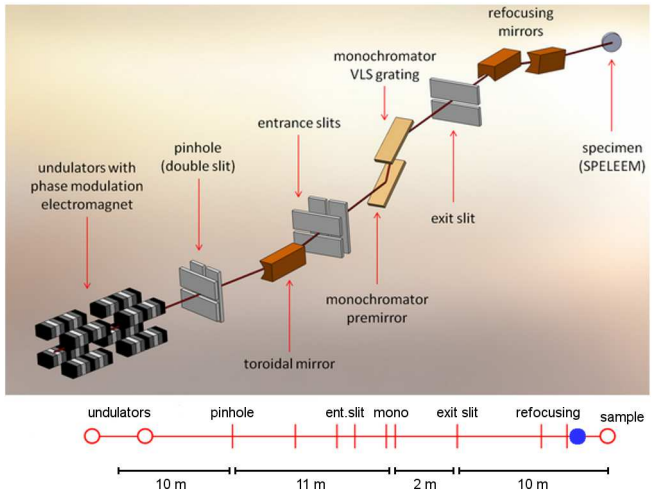


Figure 1: Schematic view of the Nanospectroscopy beamline at Elettra. Distances between the relevant elements are shown on the bottom. The blue circle just before the sample represents the position of the coherence defining filter, which is 770 mm upstream of the sample.

vertical and horizontal slits at the start of the beamline defining the source.

The monochromator consists of 3 different gratings in order to cover the entire soft x-ray energy regime. The two VLS gratings are of 400 lines/mm and 200 lines/mm for higher and lower photon energies, respectively. The third grating has a spherical profile with 10 lines/mm and is intended only for the lower photon energies below 50 eV. The monochromator also includes a plane mirror, as well as entrance and exit slits placed 2 m before and after the gratings, respectively [9].

The monochromatized photon flux on the sample is in the range $10^{12} - 10^{13}$ photons/s depending on the photon energy and the slit openings. The maximum flux is obtained at about 150 eV. The two elliptical refocusing mirrors in the Kirkpatrick-Baez configuration provide a focal spot on the

sample both in the horizontal and vertical directions [9]. The x-ray beam size on the sample is measured to be about 7 $\mu m \times 2\ \mu m$ (hor $\times$ ver). Considering that the beam is incident on the sample at 16° from the surface plane in the horizontal direction, the beam footprint on the sample is about 25 $\mu m \times 2\ \mu m$ at best [10]. Apart from the adjustable bending of the mirrors used for optimizing the focus, pitch of the two mirrors are used for moving the x-ray beam on the sample.

### *2.2. SPELEEM*

The current study utilizes mainly the Spectroscopic PhotoEmission and Low Energy Electron Microscope (SPELEEM) installed at the Nanospectroscopy beamline. This instrument combines x-ray photoemission electron microscopy (XPEEM) and low-energy electron microscopy (LEEM) [12]. XPEEM provides chemical and magnetic information [13], whereas LEEM probes the crystal structure as well as surface work function in a laterally-resolved manner [14, 15].

The SPELEEM instrument is sketched in Fig. 2a. As mentioned in the previous section, the x-ray beam is incident on the sample surface at 16° grazing angle. In the XPEEM operation, the photoemitted electrons are collected along the surface normal, which coincides with the electron-optical axis of the microscope. Instead, in the LEEM operation, the electron beam is generated by an $LaB_6$ source, and the incident and reflected electron beams are deviated using a magnetic separator. In both operation modes, the electron energy ranges from a few eV up to hundres of electron volt. A negative high voltage bias at the sample accelerates the electrons into the imaging column. The hemispherical energy analyzer (EA) is used in filtering the photoelec-

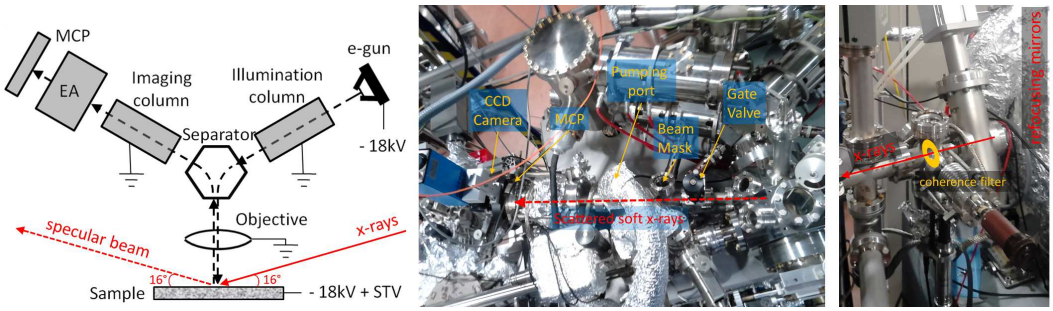


Figure 2: a) Sketch of the SPELEEM instrument is shown. The black lines indicate the electron trajectories, whereas the red lines correspond to the incident and scattered photon beams. b) Photo of the diffraction chamber is shown. The dashed red line correspond to the x-ray beam scattered along the specular direction. An area detector is used to collect the speckle pattern around the specular beam. c) A coherence-defining aperture is placed xxx m upstream of the sample. The linear feedthrough (seen on the bottom right of the photo) is used to switch between different size pinholes, whereas a bellow stage is used to fine-adjust the pinhole on the beam axis.

tron energies, whereas the multichannel plate area detector coupled with a phosphor screen and a CCD camera gives a magnified image of the electrons emitted (XPEEM) or reflected (LEEM) from the surface.

The microscope provides a lateral resolution of about 10 nm in LEEM mode and 30 nm in XPEEM mode [16]. The surface sensitivity is given by the electron escape depth, which is less than a few nanometers for the low electron energies considered here [17]. The chemical contrast in XPEEM comes from the laterally-resolved x-ray absorption and photoemission spectroscopies. The magnetic contrast instead is provided by the enhanced interaction cross-section of x-rays with a magnetic moment at particular absorption thresholds. This interaction can be extracted taking a difference between right and left circularly polarized x-rays [18]. Such a signal extracted from

a polarization analysis, termed as circular dichroism, is proportional to the component of net magnetization along the beam propagation direction.

### *2.3. X-ray diffraction measurement within the SPELEEM setup*

Among other processes such as photoemission and fluorescence, part of the incident x-rays are elastically scattered. Considering reflection from a mirror-like surface, the highest intensity for scattering is found in the specular direction. In the case of a coherent plane wave incident on the sample, a speckle pattern (i.e. diffraction from an irregular object) is expected at around the specular beam. In a typical diffraction measurement, the diffraction pattern is acquired by using an area detector. Size of the speckles on the detector reflects the size of the illuminated sample. Total solid angle collected on the area detector, instead, reflects the smallest sample features that contribute to the diffraction pattern. Therefore, the pixel size and the total area of the detector determine the maximum field-of-view and the spatial resolution, respectively, in reconstructed real-space images using CDI.

Electron optics in the SPELEEM instrument are placed along the surface normal as sketched in Fig. 2a, which allows the specularly-reflected x-ray beam at near grazing angles to be simultaneously measured on a separate detector. This was implemented by attaching an extension chamber to the existing SPELEEM setup as shown in the photo in Fig. 2b. Most prominently, this chamber features an MCP detector of 40 mm diameter for direct x-ray detection, place at a 740 mm distance from the sample. Identically to the electron measurement in the XPEEM setup, the MCP is coupled to a phosphor screen, which is subsequently imaged onto a CCD camera. The channel plate covers about 900 pixels on the CCD. Apart from the detec-

tor, there is a central beam mask placed on a linear feedthrough in order to protect the detector from the specular beam.

The level of coherence from the two undulator sources was measured previously by using another CDI setup, temporarily installed at the Nanospectroscopy beamline [19]. The level of coherence was found from the fringe visibility in the interference pattern between two pinholes with varying separation. At low photon energies, at or below 250 eV, an almost fully coherent beam was observed up to 11 $\mu$m pinhole separation, whereas at higher photon energies, the lateral coherence length is substantially lower. In order to assure an adequate level of coherence up to the L edges of 3d transition metals, we have placed a coherence defining filter between the refocusing mirrors and the sample, as shown in Fig. 2c. The filter used in the following measurements is a 500 $\mu$m square aperture located at 770 mm away from the sample. The aperture cuts the photon flux to 5% of the full beam, consistent with the size of the beam at the aperture plane, which is several mm's.

## 3. Spin-ice lattice: structure

In order to test the feasibility of the diffraction measurement within the SPELEEM setup, we have prepared spin-ice lattices constructed of Permalloy nanowires. The area relevant to the diffraction measurements is shown in the optical image in Fig. 3. Each individual lattice was limited to within about 5 $\mu$m in order to match the lateral coherence length of the beamline at the photon energies corresponding to the L edges of transition metals. The distance between different lattices was set to 200 $\mu$m in horizontal and 50 $\mu$m in vertical to avoid illuminating more than one lattice at a time. (*Here there*

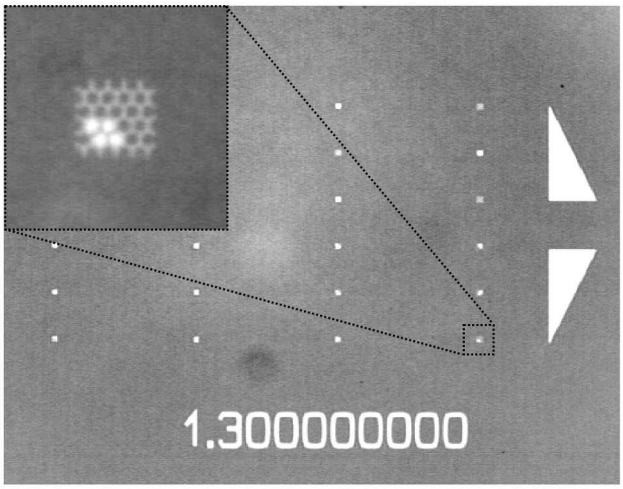


Figure 3: Optical microscopy image of the spin-ice lattice used in the measurements. The big triangles on the right are alignment marks, whereas the small dots arranged in a regular array are individual lattices. The one used in the measurements is shown in the inset in higher magnification. The size of the lattice is about 5 $\mu$m. The distance between individual arrays is 200 $\mu$m in horizontal and 50 $\mu$m in vertical.

*can be more details about the samples: the way the lithography was done, what that number 1.30000 signifies, etc.*)

As seen in the inset of Fig. 3, the imperfect lift-off process left behind residual material in some of the hexagonal cells within the lattice. The same imperfections can be recognized in the XPEEM image at the Fe $L_3$ edge shown in Fig. 4a. Importantly, the XPEEM image is mirrored with respect to the optical image, because of an additional reflection between the MCP detector and the CCD camera. The same detector configuration is used also in the diffraction measurement.

The high resolution XPEEM image in Fig. 4a shows the honeycomb lattice with connected vertices. In the inset the orientation of the lattice with respect

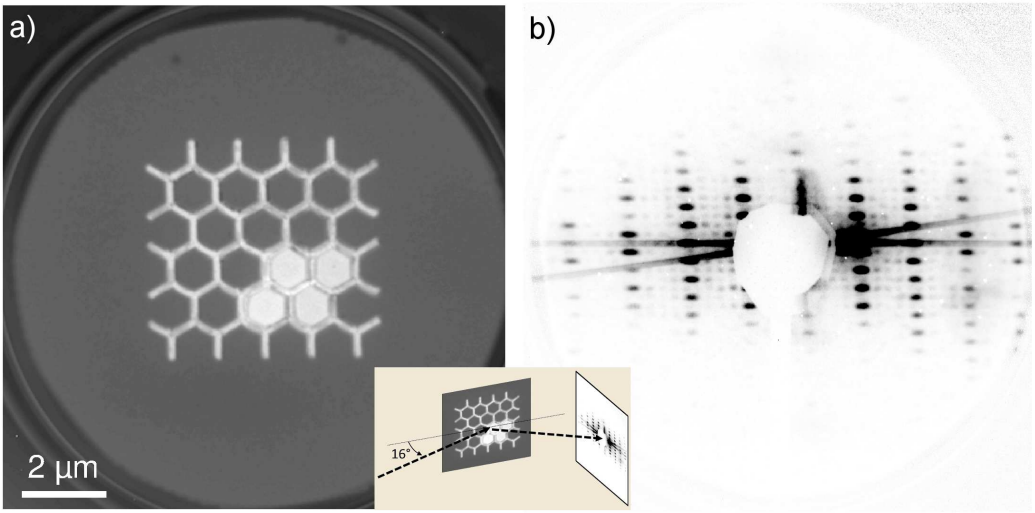


Figure 4: a) XPEEM image of the individual lattice used in the diffraction measurements. Photon energy is 707.4 eV tuned to the Fe $L_3$ edge. The photoelectrons are measured at the secondary electron peak at few eV. b) X-ray diffraction pattern measured simultaneously to the XPEEM image at the same photon energy. The inset shows the scattering geometry with 16° grazing incidence angle.

to the scattering geometry is given. The resulting diffraction pattern about the specular beam is shown in Fig. 4b. The periodic hexagonal lattice gives rise to the regular array of diffraction peaks. The two diffuse streaks of intensity in Fig. 4b, instead, are due to the tail of the beam scattering off the marker triangle nearby (see Fig. 3). The central part of the diffraction pattern is blocked by the beamstop, which also contains the slightly diverging specular beam.

Considering that the XPEEM image and the diffraction pattern originate from exactly the same region, one can use the XPEEM image to provide the missing phases in order to facilitate the real-space reconstruction of the

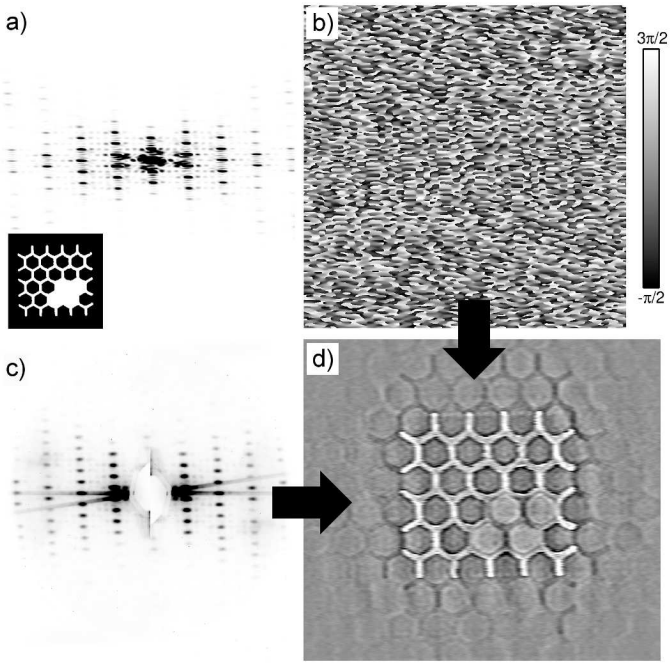


Figure 5: a) Amplitudes and b) phases of the simulated speckle pattern using the binary image shown in the inset obtained from the XPEEM image. c) Measured speckle pattern at the Fe $L_3$ edge (707.4 eV photon energy) is centrosymmetrized. d) Reconstructed real space image by using measured amplitudes and simulated phases.

diffraction image. This is illustrated in Fig. 5. The combination of measured diffraction amplitudes (Fig. 5c) with the simulated phases (Fig. 5b) obtained from the binary XPEEM image (inset) results in the real space image in Fig. 5d. The details of this reconstructed image compares well with the XPEEM image in Fig. 4a. The beamstop and the streaking diffuse light give rise to weak replicas of the honeycomb lattice in the surrounding region and negative values in certain parts of the image.

The resolution of the reconstructed image is expected to be below 100 nm based on the simple figure $L\lambda/R \approx 30$ nm using $L = 740$ mm, $\lambda = 1.75$ nm

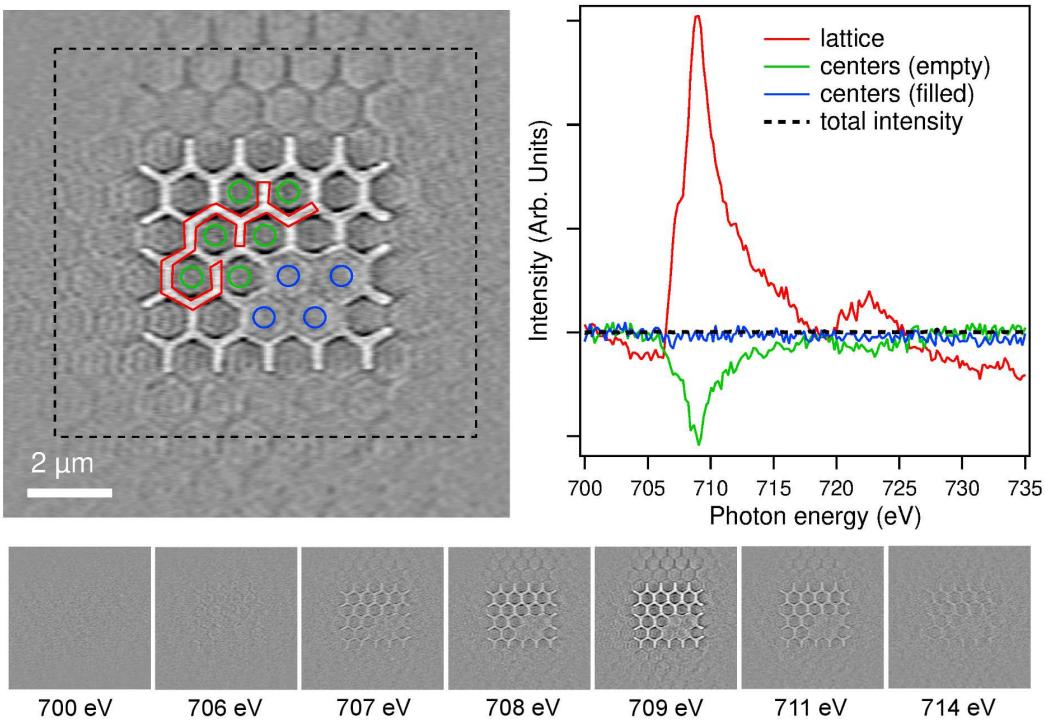


Figure 6: a) Difference of reconstructed images at 709 eV ($L_3$ peak) and at 700 eV (baseline) photon energy. b) X-ray absorption spectra extracted from the indicated regions on the image. c) Some of the reconstructed diffraction images taken from the sequence as a function of photon energy. The image at 700 eV is subtracted from all the rest.

and $R = 40$ mm. Along the direction of grazing incidence (horizontal axis in Fig. 4a), the incidence angle degrades the resolution further by a factor corresponding to $\sin 16°$. Indeed, measuring profiles across the wires, the reconstructed image in Fig. 5d is broadened with respect to the XPEEM image by about 110 nm along the horizontal direction (see Appendix).

Evidently, the reconstruction in Fig. 5d is based on the XPEEM image, and thus the resemblance is not surprising. However, once the phases are established, more information can be obtained from the diffraction mea-

surement. This idea can be demonstrated in the photon energy dependence shown in Fig. 6. Measuring the diffraction amplitudes as a function of energy and using the phases from the same binary XPEEM image (inset in Fig. 5), we obtain the reconstructed real space image across the Fe L-edge. Fig. 6 displays the baseline substracted images at the $L_3$ peak and throughout the $L_3$ edge. Importantly, the acquisition time per diffraction pattern at each photon energy was 20 s.

One can extract the x-ray absorption spectra from different parts of the reconstructed image sequence. There are a few observations to be made from the spectra in Fig. 6. Firstly, laterally-resolved absorption spectra give a strong Fe signal from the lattice itself. Moreover, a certain level of oxidation is evident from the spectra as expected from the ambient exposure. Then, the effect of the beamstop can also be observed in the negative peak within the regions which in reality do not contain any Fe. This can be understood from the fact that the central part of the diffraction pattern contains the integrated intensity in real space. The beamstop removes the angles around the specular beam, thus, the integrated intensity within the inverse transformed image should be necessarily zero. This can be seen in the total intensity as a function of photon energy (black dashed line in the XAS plot), which is identically zero throughout the absorption scan. Interestingly, the cells of the honeycomb lattice filled with a wetting layer do not show any Fe signal. This is partly because the weaker signal expected from a few layers of material compared to the rather thick wires constituting the lattice. Also important is the fact that due to their larger extent in real space the diffracted intensity from the cells ends up mostly behind the beamstop.

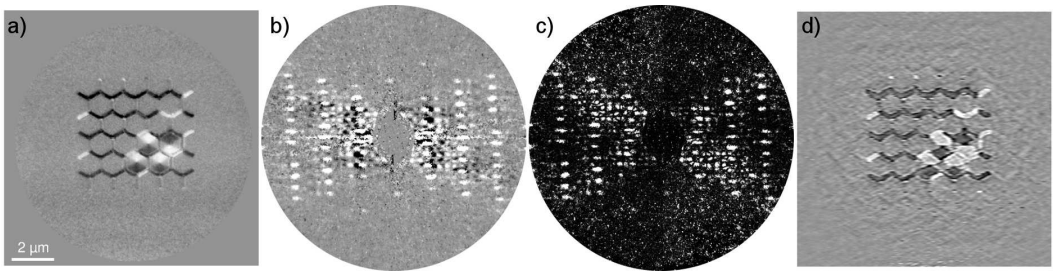


Figure 7: a) XMCD-PEEM image of the spin-ice lattice at 707.4 eV photon energy. b) Dichroic part of the diffraction pattern at 707.4 eV obtained by taking the difference between measurements with left and right circularly polarized x-rays. c) Approximated magnetic scattering amplitude as explained in the text. d) Resulting magnetic reconstruction, using the phases calculated from the XMCD-PEEM image.

## 4. Magnetic Scattering

In addition to the chemical structure depicted in Fig. 6, the spin-ice lattice shows a rather simple magnetic structure, with each wire constituting the lattice acting as a single macrospin. The magnetization map is displayed in the XMCD-PEEM image in Fig. 7a. The circular dichroic image is obtained by taking the difference of two XPEEM images with opposite circular polarizations normalized to their sum. Such a measurement is sensitive to the projection of magnetization along the beam direction. As the x-ray beam is along the horizontal direction in Fig. 7a, the vertical wires do not give any magnetic contrast. Furthermore, the filled cells on the bottom right feature vortex-like domain patterns.

In resonant x-ray scattering, charge and magnetic contributions have distinctly different photon energy and polarization dependencies [20]. Thus, one can consider the scattering amplitude in three parts corresponding to pure charge scattering, pure magnetic scattering, and the interference between the

two [21]. Defining the charge and magnetic structure factors as $F(\vec{\mathbf{K}})$ and $M(\vec{\mathbf{K}})$, respectively, the total diffracted intensity can be expressed as [20]:

$$I(\epsilon, \vec{\mathbf{K}}, \lambda) = a_{\epsilon,\vec{\mathbf{K}},\lambda}|F|^2 + b_{\epsilon,\vec{\mathbf{K}},\lambda}|M|^2 + [c_{\epsilon,\vec{\mathbf{K}},\lambda}FM^* + c.c.] \tag{1}$$

where $\epsilon$ is the photon polarization vector, $\vec{\mathbf{K}}$ is the momentum transfer and $\lambda$ is the wavelength. $a$, $b$ and $c$ are angle, energy and polarization dependent coefficients, and $c.c.$ stands for the complex conjugate of the interference term. It is easy to identify the first term with charge scattering, the second one with magnetic scattering and the last one as the charge-magnetic interference. Under small angle approximation, the coefficients of the first two terms depend only weakly on photon polarization. Therefore, magnetic scattering contribution is equally strong both for circular and linear polarization. On the other hand, the interference term can only be observed using circularly polarized x-rays, whereas it is highly suppressed for linear polarization [20]. Moreover, the coefficient $c$ changes sign between left and right circularly polarized light, thus, the interference term can be extracted by circular dichroism measurements. This charge-magnetic interference is behind the idea of magnetic holography, which has become the principal magnetic imaging method using CDI [22].

Charge-magnetic interference corresponds to the convolution of the charge and magnetic structures in real space, therefore, the dichroic diffraction pattern can in principle be used to obtain the magnetic domain distribution using the known charge structure [20]. However, the difficulties in such a deconvolution procedure makes it impractical as a viable method for magnetic reconstruction. Thus, here, we apply the same idea in the previous section to magnetism, and combine XMCD-PEEM and magnetic scattering.

Magnetic scattering factor can be most easily found from the polarization dependence of the interference terms in Eq. 1. The dichroic part of the diffraction pattern from the spin-ice lattice (i.e. the difference in diffraction between left and right circular polarization) is shown in Fig. 7b. In order to obtain the amplitudes of the magnetic structure factor (i.e. fourier transform of the magnetization distribution), we divide the squared magnitude of this dichroic diffraction pattern by the total diffraction intensity seen in Fig. 5c. The resulting amplitudes are shown in Fig. 7c. Recovering the missing phases from the XMCD-PEEM image and applying a few cycles of iterative refinement, we obtain the reconstructed magnetic domains in Fig. 7d. The iterative refinement applies to the diffraction amplitudes and helps to partially recover the missing part behind the beamstop (for the reconstructed image before iterative refinement see Appendix).

In the inverse transform of the magnetic diffraction, the same features as in the XMCD-PEEM image can be clearly recognized. Note that trials in which we use different combinations between measured amplitudes and simulated phases are shown in the Appendix. Clearly, the simulated phases are crucial in obtaining a sensible image. Nevertheless, we note that the amplitudes are identified correctly and the magnetic scattering is extracted reliably.

## 5. Conclusions

In the preceding sections, we demonstrated the successful implementation of coherent diffraction measurements in reflection geometry within an existing XPEEM setup. Moreover, the simultaneously-measured XPEEM

images were used to obtain simulated diffraction patterns, which were perfectly matched to the experimental diffraction data. The correct matching between measured diffraction amplitudes and simulated diffraction phases was demonstrated by the excellent match between the images transformed into real space and the XPEEM images used to simulate the phases. Moreover, the magnetic sensitivity in resonant x-ray scattering at the Fe $L_3$ edge was used to apply the same procedures to the magnetization distribution.

Evidently, having real-space images available from XPEEM, the reconstruction of the diffraction intensities appears as a rather trivial exercise. On the other hand, this exercise is fundamental in the correct interpretation and sorting of the diffraction intensities. Indeed, we expect that such an interpretation will be of great value in measurements as a function of electric and magnetic fields, under which electron-based XPEEM measurement faces great difficulty.

## 6. Acknowledgments

## Appendix A. Spatial resolution

In order to evaluate the resolution in real space of the inverse transformed diffraction patterns, we have considered a profile across the wires of the spin ice lattice. Fig. A.8 shows the intensity profiles obtained from the XPEEM and CDI images along the beam direction. The artifacts due to the inverse transform from the diffraction pattern with limited angular range are immediately apparent as oscillatory features in the background. Moreover, the relative width of the XPEEM and CDI profiles across the two wires, which appear as bright peaks, allow to estimate an additional broadening of 110 nm

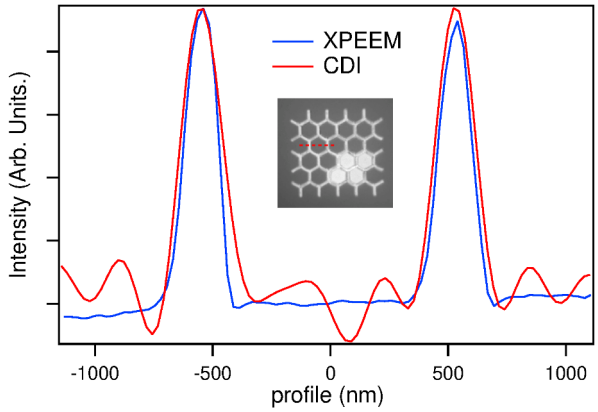


Figure A.8: Intensity profile extracted from the XPEEM and CDI images across the profile marked by a dashed horizontal line in the inset.

in CDI due to its limited solid angle. Note that the solid angle can be adjusted by changing the detector-sample distance. Nevertheless, the decision on this distance remains as a compromise between spatial resolution (which requires the detector to be close to have a larger solid angle) and speckle visibility or field-of-view (which favors the detector to be far away to have larger features).

## Appendix B. Different amplitude-phase combinations

As explained in the main manuscript, in the inverse transformation of the diffraction amplitudes require the simulated phases from the XPEEM image. We have tried also different combinations between charge/magnetic scattering amplitudes and the simulated phases of the charge/magnetic images obtained by XPEEM. The results are summarized in Fig. B.9.

Clearly, the simulated phases from the XPEEM images greatly imprint on the details of the reconstructed images. This is most evident in the com-

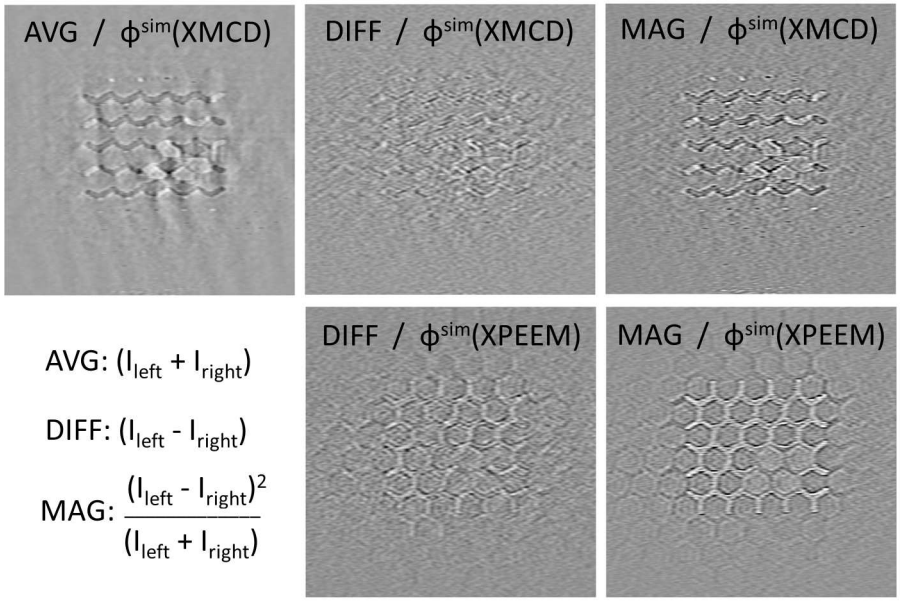


Figure B.9: Different combinations between measured diffraction amplitudes and simulated phases.The significance of AVG, DIFF and MAG are given in the bottom-left. The phases $\phi^{sim}$ are obtained either from the chemical (XPEEM) or magnetic (XMCD) photoemission image.

bination of total diffracted intensity (AVG) and simulated phases from the XMCD-PEEM image ($\phi^{sim}$(XMCD)). The total intensity is proportional to $|F|^2 + |M|^2$, and interestingly the XMCD-PEEM image, which is the source of the simulated phases, is reproduced in the inverse transform. Therefore, there is reason to conclude that the magnetic phases match with the part of intensity originating from the magnetic structure factor (i.e. $|M|^2$), and result in an image similar to the magnetic map. On the other hand, the dichroic diffraction (DIFF) does not produce any sensible image regardless of the origin of the simulated phases.

## References


[1] K. Wakabayashi, A. Kakizaki, Y. Siota, K. Namba, K. Kurita, M. Yokata, H. Tagawa, Y. Inoko, T. Mitsui, E. Wada, T. Ueki, I. Nagakura, T. Matsukawa, J. Phys. Soc. Japan 44 (1978) 1314.

[2] D. Sayre, in: M. Schlenker, M. Fink, J. P. Goedgebuer, C. Malgrange, J. C. Vieénot, R. H. Wade (Eds.), Imaging Processes and Coherence in Physics, Springer Berlin Heidelberg, Berlin, Heidelberg, 1980, pp. 229–235.

[3] J. Miao, P. Charalambous, J. Kirz, D. Sayre, Nature 400 (1999) 342.

[4] D. Sayre, Acta Cryst. 5 (1952) 843.

[5] J. Miao, T. Ishikawa, I. K. Robinson, M. M. Murnane, Science 348 (2015) 530.

[6] S. Marathe, S. S. Kim, S. N. Kim, C. Kim, H. C. Kang, P. V. Nickles, D. Y. Noh, Optics Express 18 (2010) 7253.

[7] S. Roy, D. Parks, K. A. Seu, R. Su, J. J. Turner, W. Chao, E. H. Anderson, S. Cabrini, S. D. Kevan, Nature Photonics 5 (2011) 243.

[8] T. Sant, D. Ksenzov, F. Capotondi, E. Pedersoli, M. Manfredda, M. Kiskinova, H. Zabel, M. Kläui, J. Lüning, U. Pietsch, C. Gutt, Scientific Reports 7 (2017) 15064.

[9] D. Cocco, M. Marsi, M. Kiskinova, K. C. Prince, T. Schmidt, S. Heun, E. Bauer, Proc. SPIE 3767 (1999) 271.

[10] A. Locatelli, A. Bianco, D. Cocco, S. Cherifi, S. Heun, M. Marsi, M. Pasqualetto, E. Bauer, J. Phys. IV 104 (2003) 99.

[11] L. Tosi, B. Diviacco, F. Iazzourene, R. Roux, R. P. Walker, D. Zangrando, in: Proceedings of EPAC 2000, p. 2349.

[12] A. Locatelli, L. Aballe, T. O. Menteş, M. Kiskinova, E. Bauer, Surf. Interface Anal. 38 (2006) 1554.

[13] A. Locatelli, E. Bauer, J. Phys.: Condens. Matter 20 (2008) 093002.

[14] E. Bauer, Rep. Prog. Phys. 57 (1994) 895.

[15] E. Bauer, Surface Microscopy with Low-Energy Electrons, Springer-Verlag New York, 2014.

[16] T. O. Menteş, G. Zamborlini, A. Sala, A. Locatelli, Beilstein J. Nanotechnol. 5 (2014) 1873.

[17] S. Tanuma, C. J. Powell, D. R. Penn, Surface and Interface Analysis 43 (2011) 689–713.

[18] C. M. Schneider, G. Schönhense, Rep. Prog. Phys. 65 (2002) R1785.

[19] E. Pedersoli, F. Capotondi, D. Cocco, M. Zangrando, B. Kaulich, R. H. Menk, A. Locatelli, T. O. Mentes, C. Spezzani, G. Sandrin, D. M. Bacescu, M. Kiskinova, S. Bajt, M. Barthelmess, A. Barty, J. Schulz, L. Gumprecht, H. N. Chapman, A. J. Nelson, M. Frank, M. J. Pivovaroff, B. W. Woods, M. J. Bogan, J. Hajdu, Review of Scientific Instruments 82 (2011) 043711.

[20] T. O. Menteş, C. Sánchez-Hanke, C. C. Kao, Journal of Synchrotron Radiation 9 (2002) 90–95.

[21] A. Rahmim, S. Tixier, T. Tiedje, S. Eisebitt, M. Lörgen, R. Scherer, W. Eberhardt, J. Lüning, A. Scholl, Phys. Rev. B 65 (2002) 235421.

[22] S. Eisebitt, J. Lüning, W. F. Schlotter, M. Lörgen, O. Hellwig, W. Eberhardt, J. Stöhr, Nature 432 (2004) 885–888.